Measuring the Velocity of Fluorescently Labelled Red Blood Cells with a Keyhole Tracking Algorithm

C.C. Reyes-Aldasoro[1], S. Akerman and G.M. Tozer

Abstract **In this paper we propose a tracking algorithm to measure the velocity of fluorescently labelled red blood cells (RBC) travelling through microvessels of tumours, growing in dorsal skin flap window chambers, implanted on mice. Pre-processing removed noise and artefacts from the images and then segmented cells from background. The tracking algorithm is based on a 'keyhole' model that describes the probable movement of a segmented cell between contiguous frames of a video sequence. When a history of cell movement exists, past, present and a predicted landing position of the cells will define two regions of probability that resemble the shape of a keyhole. This keyhole model was used to determine if cells in contiguous frames should be linked to form tracks and also as a post-processing tool to join split tracks and discard links that could have been formed due to noise or uncertainty. When there was no history, a circular region around the centroid of the parent cell was used as a region of probability. Outliers were removed based on the distribution of the average velocities of the tracks. Since the position and time of each cell is recorded, a wealth of statistical measures can be obtained from the tracks. The algorithm was tested on two sets of experiments. First, the vasculatures of eight tumours with different geometries**

[1] Corresponding Author:
Address: Cancer Research UK Tumour Microcirculation Group,
Academic Unit of Surgical Oncology, The University of Sheffield,
K Floor, School of Medicine & Biomedical Sciences
Beech Hill Road Sheffield S10 2RX, UK
Email c.reyes@sheffield.ac.uk
Telephone 0 114 27 12850

were analysed; average velocities ranged from 86 to 372 [μm/s], with minimum and maximum track velocities 13 and 1212 [μm/s], respectively. Second, a longitudinal study of velocities was performed after administering a vascular disrupting agent to two tumours and the time behaviour was analysed over 24 hours. In one of the tumours there is a complete shutdown of the vasculature while in the other there is a clear decrease of velocity at 30 minutes, with subsequent recovery by 6 hours. The tracking algorithm enabled the simultaneous measurement of RBC velocity in multiple vessels within an intravital video sequence, enabling analysis of heterogeneity of flow and response to treatment in mouse models of cancer.

Keywords— Red Blood Cell Tracking, Keyhole Tracking Model, Blood Flow, Tumour Vasculature.

INTRODUCTION

Intravital microscopy allows direct observation of red blood cell (RBC) movement in microvessels of small animals under both normal and pathological conditions (Sandison, 1924, Algire, 1943, Algire & Legallais, 1949, Branemark & Lindstrom, 1963). The analysis of RBC movement and velocity is of great interest in many areas of research, for example, the RBC velocity before and after a treatment can contribute to the responsiveness to vasoactive drugs (Prazma *et al.*, 1989), the distribution and flow of RBCs in cerebral microvessels can be used to measure oxygen tension (Tsukada *et al.*, 2004) or the velocity can be used to estimate hydrodynamic wall shear stress (Vennemann *et al.*, 2006). RBC velocity can also be used as a

measure of response to vascular disrupting agents in cancer research (Tozer *et al.*, 2001). The tumour vasculature has become an attractive target for therapy because the provision of oxygen and nutrients by a single vessel supports the proliferation and survival of many tumour cells and it provides a main route for metastatic spread. Vascular disrupting agents (VDAs) are a new class of anti-cancer drugs that are aimed at causing rapid and selective shutdown of the established tumour vasculature, leading to secondary tumour-cell death (Tozer *et al.*, 2005b).

Despite its importance, the off-line measurement of RBC velocity from a dynamic sequence of images captured from intravital microscopy preparations has been restricted mainly to 1D or 2D cross-correlation or even manual measurements of distances over a screen (Tozer *et al.*, 2001). Particle Image Velocimetry (PIV) (Sugii *et al.*, 2002, Tsukada *et al.*, 2000) relies on the 2D cross-correlation between “investigating windows” (small, fixed-size regions of interest within an image) which allows the measurement of the relative movement of the intensities inside the window between time-frames. This analysis is restricted to simple geometries, like a single vessel, since more complicated geometries could result in incorrect measurements due to aliasing, flows in opposite directions or other artefacts. Kymographs (Salmon *et al.*, 2002, Waterman-Storer *et al.*, 1998, Japee *et al.*, 2005, Ji & Danuser, 2005) (sometimes called Space-Time Images) rely on 1D cross correlation of the intensities described by a manually-traced line over an image in consecutive frames. This analysis is thus restricted to a single straight line, or at the most a collection of straight lines, and does not consider orientations but only relative movement within a line.

A proper tracking algorithm that traces the course or 2D movements of individual RBCs from frame to frame can provide more information than kymographs or PIV, by obtaining data from multiple blood vessels, in different orientations, within a region of observation. For this purpose, the RBCs need to be segmented from each video frame and their positions need to be identified in so-called pre-processing steps. Methodologies to track leukocytes with active contours and Montecarlo methods have been presented in (Cui *et al.*, 2006, Ray *et al.*, 2002, Acton *et al.*, 2002) where the shape and size of a leukocyte are used to track its movements adequately, yet these algorithms are restricted to the analysis of a single leukocyte of interest. A complete methodology to track circulating fluorescent particles is presented in (Eden *et al.*, 2005). The algorithm requires many pre- and post processing steps (edge-based registration of the frames to compensate for mesenteric movements, texture and temporal-based segmentation of the vessels to restrict the correspondence of objects between frames, calculation of optical flow to resolve uncertainties, colour-feature segmentation of the cells and model-based motion correspondence), which require user interaction like manual initialising or testing and training of Artificial Neural Networks.

In this study, we developed a tracking algorithm based on a ‘keyhole’ model that describes the probable movement of fluorescently labelled RBCs travelling within tumour vascular networks and links RBCs on contiguous frames to form tracks that span over the analysed frames. The algorithm relies on fluorescence labelling to enable the segmentation of the RBCs. ‘Keyhole’ relates the shape of two regions that when put together resemble a traditional door keyhole. A series of post-processing steps are required to

minimise the effect of uncertainty in the linking process, to discard tracks that may arise from noise and to join split tracks. The algorithm requires minimal user intervention, does not require training data or sophisticated pattern recognition techniques and is capable of analysing complex vascular networks with RBCs travelling simultaneously in different directions.

We used the algorithm to investigate tumours with different vascular architectures and the effect of the VDA, disodium combretastatin-A-4 3-*O*-phosphate (CA-4-P) on RBC velocity in murine tumours expressing only single isoforms of the important pro-angiogenic growth factor, vascular endothelial growth factor (VEGF). The most prevalent isoforms of VEGF are VEGF120, VEGF164 and VEGF188 in the mouse. Transgenic mice expressing only one of these isoforms have helped establish that expression of VEGF120 alone is associated with poorly developed and leaky blood vessels in normal tissues, whereas VEGF188 is associated with recruitment of peri-endothelial support cells and complex vascular networks. VEGF164 tends to have intermediate effects (Carmeliet & Collen, 2000, Stalmans *et al.*, 2002). The tumour cell lines used in the current study express either VEGF120 alone or VEGF188 alone and present very different vascular morphology and function, when grown as solid tumours *in vivo* (Akerman *et al.*, 2006). Thus we hypothesized that the different tumour types would respond differently to VDA treatment and provide a range of red cell velocities for testing the proposed tracking algorithm. RBC velocity was assessed for a 24-hour period after a single moderate dose of CA-4-P.

MATERIALS AND METHODS

Window chambers

Intravital microscopy was carried out in tumours implanted into dorsal skin-flap "window" chambers in mice, as described previously (Tozer et al., 2005a). Briefly, an aluminium window chamber weighing ~2g, with a single glass window in place, was surgically implanted into a depilated skin flap and a tumour fragment was placed onto the surgically exposed subcutaneous panniculus muscle within the chamber. The chamber was closed by placement of the second glass window, providing a depth of approximately 200 μm for tumour growth. Animals were given appropriate post-operative treatment to aid recovery and then kept in a warm room, 28-30 ^{o}C, until the day of experiment.

Red blood cell labelling

Donor red blood cells were obtained by cardiac puncture from anaesthetized donor mice, as published previously (Unthank *et al.*, 1993). Briefly, RBCs were separated from blood plasma and white blood cells by centrifugation and the isolated and washed RBCs incubated with a membrane dye, DiI (Molecular Probes – Invitrogen UK) for 30 mins. 25 μg of DiI was used per 50 μl of packed RBCs. After incubation, the RBCs were washed and resuspended in phosphate buffered saline (50 μl ml^{-1} red blood cell-DiI complex).

Intravital microscopy and video sequences

Intravital microscopy was carried out approximately 6-10 days after surgery, when tumours reached approximately 3.5 mm in diameter. A Nikon Eclipse

E600FN fluorescence microscope with a x20 zoom and modified stage to take mice was used. Animals were placed on the stage in a custom built restrainer such that the window chamber was located adjacent to the objectives in a fixed position. The microscope was set up to view the tumour preparations under epi-fluorescence illumination using a 100 W mercury arc lamp for measurement of RBC velocity. Fluorescence was set up to excite at 550 nm and detect the emissions at 565 nm from the DiI-labelled cells. Each animal received 0.1-0.2 ml of labelled RBCs made up at a concentration of 50 μl DiI labelled RBCs/ml via the tail vein. Video observations were recorded in digital format, using a Sony DSR-30P digital videocassette recorder that records at 25 frames per second (fps) for off-line analysis.

For demonstrating the algorithm in tumours with different vascular architectures, video sequences of a maximum of 500 frames from each of 8 tumours with different vasculatures were selected from a range of single VEGF isoform expressing tumours with no drug treatment. A longitudinal study was designed to investigate the effect of the tumour vascular disrupting agent, CA-4-P on tumour RBC velocity. A single VEGF120-expressing and a single VEGF188-expressing tumour were observed before CA-4-P was administered and at the following time points: 2.5, 15, 30, 60 [minutes], 3, 6, 24 [hours]. Two separate regions of interest were observed in each tumour, resulting in 4 series of measurements, with 8 time points in each. At each time point, 60 frames were analysed. The resulting tracks made by the fluorescent RBCs were manually validated. This involved visual examination of each track to determine whether the cells linked by the algorithm corresponded to the

same cell moving from frame to frame (correct) or if they were the product of different cells or noise (incorrect).

DESCRIPTION OF THE TRACKING ALGORITHM

The tracking algorithm consisted of three main steps: *pre-processing* which transformed the acquired videos into a sequence of suitable binary images containing segmented foreground objects; *tracking*, which linked the objects in contiguous frames to form the tracks; and *post-processing* which removed links in tracks that could have resulted from noise and joined sections that were considered to be split sections from a single track.

Reduction of the computational complexity

One second of video (at 25 fps, 576 rows and 720 columns) yields more than 10 million pixels and so it is important to reduce the computational complexity of processing a video. We reduced the number of pixels by a factor of 4 by discarding alternate rows of each image and then, for every row, 2 contiguous pixels were averaged and their mean value used to create a new pixel, thus reducing the columns by half. This process is similar to a standard *quad tree* averaging (Gaede & Günther, 1998). Besides the dimension reduction, this averaging provides local smoothing. The general effect of the local averaging is an increase on the certainty of the intensities, which improves the segmentation, against an increase of the uncertainty of the position, which could impact on the velocity. Since the distances are calculated on the centroid of the cells, we do not consider that the averaging has a considerable impact on the velocity.

Removal of artefacts

First, it was necessary to remove any artefacts, such as intensity inhomogeneity, noise, and any labels that have been super-imposed on the images during acquisition. A *mean image* of a sequence of images was obtained by averaging the intensity values from every pixel of the whole sequence of images. The mean image was then subtracted from every frame to remove the artefacts. This process is shown in figures 1 (a-c).

Next, a suitable fluorescence intensity threshold was selected to segment a number of foreground objects (that is, the RBCs themselves) from the background; this is the only manual intervention required from the user (figure 1 (d, e)). Although the segmentation may exclude several objects whose brightness is below the threshold level, this is not critical for the tracking since it will exclude some tracks corresponding to relatively dark RBCs. Once the binary images were obtained a unique label was assigned to each of the objects. In figure 1 (f) each labelled object is represented by a different shade. Finally, the centres of gravity or centroids of the objects were obtained together with the distances that separated them from their neighbours, if any.

Tracking of the red blood cells

A keyhole model was developed to perform the tracking of the fluorescently labelled RBCs. The model arose from the observation of the movement of RBCs in the tumour vasculature: the most probable step for a RBC that is moving from frame *t-1* to frame *t*, is to follow the direction of the previous steps with the same velocity to frame *t+1*. If we assume that a child RBC (cell at frame *t*) will move with exactly the same direction and velocity as its parent (same cell at frame *t-1*), we can predict its landing position for the next frame. Of course, this would not cover changes in speed, turns in vessels or even

simple movements within a wide vessel. We therefore defined two regions of probability, a narrow wedge (60° wide) oriented towards the predicted landing position, and a truncated circle (300°) that complements the wedge; together they resemble a keyhole (figure 2). The radius of the wedge was longer (3 x parent-child distance) than that of the circle (0.5 x parent-child distance) to capture objects that increased their speed. Similarly, the circle would capture RBCs that changed direction but only those that are close to the parent. In this way, parent-child relationships are restricted to objects that are relatively close to their parents or that follow the previous movements. This model can only be assumed if there is a previous history of movements of the RBCs, which of course introduces uncertainty into the relationship assigned, but this will be tested later in the post-processing (see below). When there was no history to determine the size of the circular region, the radius was determined by 50% of the minimum distance between neighbouring objects. If there is just one object in the frame and no history, then the radius will be arbitrarily assigned as the number of columns or rows, whichever is smaller, divided by 4.

The algorithm involves linking objects between consecutive frames based on the following criteria: when the algorithm begins, all the objects look for a possible child in the next frame within a circular region around their own position; those who find a child will be linked. When an object has been linked to another object in a previous frame, they form a track and the keyhole model is used to look for a child within the keyhole in the following frame. In case a RBC lands in two different keyholes, it will be linked to the keyhole whose predicted landing position is closest. In the case that more than one RBC land

within one keyhole, the one closest to the predicted landing is selected. Once all segmented RBCs have been examined for possible parent-child relationships, a reduced number of them will have formed a series of tracks of different lengths. Figure 2 (e) exemplifies the tracking algorithm with two tracks of different velocities.

Post-processing of tracks

Post-processing of the tracks consisted of four steps: analysis of the first link of each track, linking of disjointed tracks, removal of short tracks and removal of outliers. First, for every track, the first or top RBC (time *t*) would have been assigned as a parent without any previous history of movements, thus it is possible that it was incorrectly assigned to the track. This was tested by analysing the movement backwards. That is, the same keyhole model used child (*t+1*) and grandchild (*t+2*) to generate a keyhole at time (*t*). If the top RBC was found to land inside the keyhole, it remained as part of the track, otherwise it was removed.

Next, tracks that appeared to be split artefactually, perhaps as a result of noise or incorrect segmentation, were tested for linkage by a similar backwards analysis. For every track, we generated a keyhole with its top two RBCs. If the bottom RBC of another track landed within the keyhole, the tracks were linked.

Then it was assumed that longer tracks were more reliable than smaller tracks. Tracks that have only 2 or 3 RBCs linked between frames were considered unreliable and deleted from further analysis.

The last post-processing step was to discard outliers, those tracks whose average velocity exceed 3 times the standard deviation from the mean

average velocity of the whole distribution were discarded. The mean average velocity was calculated as a weighted average of the velocity by their length in order to compensate for the fact that long tracks (which can span up to 500 frames) will tend to have lower average velocities than shorter tracks. So the weighted average or expected value of the velocity is given by:

$$E(x) = \frac{\sum_i velocity(i) \times length(i)}{\sum_i length(i)}$$

where i represents every track and $E(x)$ is the expected value of the velocity. The standard deviation is obtained by:

$$Std(x) = \sqrt{\left(E(x^2) - E(x)^2\right)}.$$

RESULTS

Vasculature analysis experiment

This experiment was performed to test the algorithm and to observe the different vasculatures described by the velocity of RBCs travelling through eight different tumours. The corresponding tracks with their average velocities are presented in figure 3. The average velocity of each branch determined their colour; dark blue corresponds to the vessels with slowest RBCs and red-brown corresponds to vessels through which the fastest RBCs were travelling. The geometry of the tumour vasculature can be observed clearly from the tracks together with the varying velocities of the RBCs. In figure 3 (a) it can be seen that there are several rather straight and narrow vessels with few curves, while in the other figures vessels tend to be more tortuous and curvilinear. It can be seen that even within one tumour, the velocity of different

vessels can be quite dissimilar; this is particularly noticeable in 3 (a, b, d, and g) where some vessels tend to have fast RBCs while others have only slow ones. In 3 (a) for instance, a “fast” vessel can carry RBCs that travel at 500-700 [μm/s] (long straight on the left), while a “slow” vessel can have RBCs moving at 15-120 [μm/s] (“J” shaped in the top centre). In general the tracks show heterogeneity of flow, which is well-known in tumours (Fukumura & Jain, 2006). The velocity for each of the eight tumours analysed ($E(x)\pm Std$) is presented in table 1 together with the maximum and minimum track velocities. The average velocity for all the 8 sets is 230 [μm/s] with a range 7-1082 [μm/s].

The tracks produced in this analysis are inherently 3D vectors [rows x columns x time], and therefore they can be plotted with different view angles, which can reveal information that is not visible in a traditional 2D time projection like the ones in figure 3. In figure 4, the tracks of two tumours, those corresponding to figure 3 (a, b) are presented with different view angles. In figure 4 (a, b) the tracks are presented in a “lateral” or column projection, where the vertical axis represents time going upwards and the horizontal axis represents the rows. The time activity of the RBCs is highlighted in this view in two ways: first, the tracks of two RBCs that travel through the same vessel at different times will appear at different “heights” while in figure 3 they were projected one on top of the other one. Second, slow tracks will have a higher slope than the faster tracks that tend to be horizontal. There are even RBCs that seem to be trapped in their positions (dark blue vertical tracks). These vertical tracks are not due to vessels perpendicular to the field of view since RBCs travelling in this direction would be out of focus as soon as they leave

the optical plane, their intensity would decrease and would not be segmented as foreground objects. In figure 4 (c) a few tracks have been selected for clarity and the angle has been shifted to a proper 3D plot where rows and columns form a base plane and time is going upwards. It is now easier to distinguish the paths of the RBCs, most of which travel left-to-right, which would correspond down-up in figure 3 (a). Notice the RBC that changed direction in the middle of its path; the track followed this RBC correctly. Figure 4 (d) presents the tracks of the second tumour in a 3D plot. The majority of the RBCs travel through a wide vessel that then branches left and right. In figure 3 (b) all these tracks appear stacked on top of each other and it is hard to distinguish their paths. Some of the tracks on the left branch then change direction very abruptly. The tracks on the right-hand side are slower than those in the centre.

The behaviour of the tracks in the whole set can also be analysed through a scatter plot of the velocity against the track length, direction, maximum distance travelled between two frames or other measurements. Figure 5 presents measurements from three different tumour in one Cartesian (velocity against length of track) and two Polar scatter plots (direction of the track corresponds to the angle of the plot and velocity of the track corresponds to its distance from the centre of the plot). Each asterisk represents a track, for which the average velocity (total distance of the hops/time) and average direction (direction from first to last point) has been calculated. Several important observations arise from these scatter plots. First, outliers are easily identifiable, such as the solitary track (which will be discarded by the algorithm) circled in red with a velocity of nearly 2500 [μm/s] in (a). This track

is clearly an outlier and was discarded from the set. Another observation is the directional behaviour of the RBC through the tumour; it can be widely spread like in 5 (b) or quite concentrated like in 5 (c). Finally, since the movement between every frame is recorded for each RBC, it is possible to obtain a wealth of information beyond the average velocity. A plot of distance per frame of the RBC or cumulative distance could be useful where, for example, velocity is being monitored over a period of time during which the conditions may change e.g. the administration of a drug.

Longitudinal study

Figure 6 presents the resulting RBC velocities for the longitudinal study. In the case of the tumour expressing only VEGF120, a considerable reduction of the RBC movement appears after a few minutes and a total shutdown of the vasculature occurs after approximately 6 hours. In the tumour expressing only VEGF188 there is also a considerable reduction of the velocity reaching its lowest point after 30 minutes but then there is a recovery and the velocities after 3 hours are comparable to the starting values. The different velocities between regions are attributed to their positions within the tumour. Figure 7 presents a light microscopy image of the whole tumour at 0, 60 min and 24 hours. Here it can be appreciated that while there is haemorrhage in the 120 tumour and no visible vasculature in the centre of the tumour at 24 hours, the 188 presents a reduction of vasculature and then a recovery after 24 hours.

All the tracks of the longitudinal study were manually validated to verify they were tracking RBCs correctly. Every link between two objects in contiguous frames could correspond either to a single cell which has traversed a certain

distance, or two different objects. The first case is providing a correct link while the second is not. All tracks were visually analysed and if there was a single link that appeared to be incorrect, the whole track was considered incorrect. For the tumour expressing VEGF188, the accuracy was 91.1% (317 correct tracks vs. 31 incorrect) and for the VEGF120 tumour it was 96.9% (246 vs. 8). The artefacts that caused 39 tracks to be considered incorrect were mainly due to groups of objects travelling very close to each other, thus having more than one object inside the keyhole and the correspondence was incorrectly assigned by the model.

It is important to consider that the velocities calculated with this algorithm, and indeed with any other method that follows objects through a sequence of 2D frames, are essentially a lower-bound estimation of the real velocity. Since the image captured by the microscope is a 2D projection of a RBC moving through a three-dimensional structure, the displacement of the RBC in the third dimension cannot be observed in the 2D image other than as a slight change of focus of the RBC. Therefore, the RBC could have travelled a longer distance than the one shown in the 2D image. Figure 8 shows this 'out-of-plane' condition for a single RBC travelling through a vessel.

Robustness of the algorithm

To analyse the robustness of the algorithm we estimated the mean velocity of all tracks in the 8 tumour sets and varied the intensity threshold levels from 10 to 28 (original = 16) and the angle of the wedge from 10° to 100° (original 60°). The sensitivity to the change in the parameters is shown in figures 9 (a,

b). It can be seen that the algorithm is very robust to small variations of the angle of the wedge; there is little change in the velocities of the sets from 40° to 100°. Below 40° the average velocity decreases, as a considerable number of cells are not included in the tracks and then the cells captured by the circle tend to outweigh those captured by the wedge. Two tumours (tumour 3 blue line with diamond marker and tumour 8 black line with circle marker) present more variation with wedge angle than the rest. The estimate of the mean of the velocity in these two cases is more sensitive to variations of the parameters of the algorithm since they have a considerably lower number of tracks, 30 and 57 against more than 200 of the other tumours. This variation is again manifest when the threshold is varied from 10 to 28. The behaviour of the other tumours is relatively stable, especially those with slower RBCs, since smaller keyholes imply a higher certainty in the assignation of correspondence between RBCs. In general, their average velocities tend to decrease as the threshold is increased. This may be due to the fact that faster cells appear fainter than slower cells as they move while the shutter of the camera is open and thus their intensity spreads along the captured image.

As an indication of the computational complexity of the algorithm presented, the computation time of the programs running with Matlab version 6.5 R13 running on a Mac PowerBook G4 OS X (10.3.9) platform was measured. The times for the pre-processing, tracking and post-processing of a 500-frame video (corresponding to the tumour of figure 3 (a)) were 17.16 minutes, 4.7 minutes, and 9.4 seconds respectively. No systematic attempt to make the code more efficient was made.

DISCUSSION

The heuristic design of the keyhole model of movement is based on the observation of the movement of RBC through vasculature and when a history of previous locations exists, a predicted landing position can be calculated. From this landing position the keyhole model is constructed and correspondence between objects on contiguous frames is assigned only if they land within the two regions that form the keyhole: a circle and a wedge. The size of the keyhole varies according to the distance traversed by the RBC on the previous hop. It is important to notice that the uncertainty on the correspondence between objects grows in accordance to the size of keyhole since a higher number of RBCs can land in a keyhole with larger area. This adaptive nature of the model movement is more flexible than fixed-size sliding windows proposed in the literature and adapts to fast and slow flows. Another strength of the methodology is to apply this keyhole in a forward linking together with a backward analysis in which links can be removed or tracks can be merged. When simpler models such as a circle around the RBC or a square sliding window are used, the algorithms become more complicated and require extra steps, such as using Artificial Neural Networks, which need to be trained (Eden *et al.*, 2005), or complicated gain functions based on directional and speed coherence that need initialising (Shafique & Shah, 2005) to resolve the uncertainties of the correspondence between objects.

It should be noted that the algorithm builds on the strength of the imaging procedures: the window chambers and the fluorescent labelling of the RBCs.

The window chambers restrict the movement of the tissue within the observation periods and therefore registration is not required. The labelling of the RBCs with fluorescent DiI is very important, first because this procedure allows their recognition by an intensity-based segmentation method and second, because among all the RBCs that travel through the vasculature just a small proportion of them has been labelled. If individual RBCs were to be identified under light microscopy shape-based methods such as Condensation (Isard & Blake, 1998) would be required and it may be possible to use more sophisticated methods such as the one proposed in (Shafique & Shah, 2005) to assign the correspondences between the RBCs. The use of fluorescently labelled RBCs means that the interaction between RBCs cannot be observed. It is possible that RBCs clump together, either labelled-labelled, which would create a single brighter cell; labelled-unlabelled, which would appear as a single labelled cell; or unlabelled-unlabelled, which would not be observed. These interactions cannot be distinguished under the current imaging modality and the algorithm has no way of considering this problem. However, where clumping occurs, a reduction in velocity would be expected (Lominadze & Mchedlishvili, 1999) and this would be detected by the current algorithm. Careful comparison of consecutive fluorescent and transmitted light video sequences would be required for determining whether clumping is the cause of a decrease in velocity.

The geometry of the functional vessels of the tumour can be observed from the tracks, which is important since a conventional light microscopy image of fixed tissue would not reveal blood flow through a given vessel. From the

tracks, it is possible to observe how “organised” the flow through the vasculature is. This degree of organisation could be very important since it has been proposed that certain antiangiogenic agents can normalise the abnormal structure and function of tumour vasculature, which in turn would make it more efficient for oxygen and drug delivery (Jain, 2005).

The longitudinal study shows the different behaviour of the two tumours expressing different VEGF isoforms. The VEGF188-expressing tumour was much more resistant to the vascular disrupting effects of CA-4-P than the VEGF120-expressing tumour. In embryology, VEGF188 is known to contribute to vascular recruitment of cells such as pericytes, leading to vascular stabilization. This suggests that VEGF188-induced stabilization of tumour blood vessels reduces their response to CA-4-P. However, a much more detailed study would be needed to test this hypothesis. In the current context, the VEGF120 and VEGF188-expressing tumours were used solely to provide a range of RBC velocities for evaluating the tracking algorithm.

The data contained by the 3D tracks can provide a wealth of information describing the movement of the RBC through the vasculature and not just the traditional mean and standard deviation of the velocity. Several measurements, such as average velocity, number of frames or maximum distance per hop, of the tracks can be extracted and observed through scatter plots and the tracks can be observed in 2D or 3D plots. The algorithm has a series of noise reduction steps that increase the reliability of the results.

If we observe which region of probability of the model determined the link assignment, we can monitor the behaviour of the model. The majority of the

links, 64% on average for all the sets, were formed by RBCs that landed in the wedge of the keyhole, 15% corresponded to the circle complement of the wedge and 21% of the links corresponded to the circular region (no history). That is, nearly one fifth of the links corresponded to the top link of a track. The wedge could be further subdivided if it would be of interest, for instance, to determine how straight or tortuous the vessels were. If RBCs that landed inside the narrow inner wedge, say 20°, would outnumber those that landed on the outer part of the wedge, the vessels would be straighter than those with the opposite behaviour.

Finally, for the average velocity of all tracks in a tumour set, the estimate of the mean is fairly robust. This is especially noticeable when a large number of RBCs have been tracked and where the flow is slower, since a smaller keyhole introduces less uncertainty. In those tumours with more than 200 tracks, variations of ±20° in wedge angle or ±4 in intensity threshold would not report any considerable changes in the average velocity.

The system could be improved with a faster frame rate acquisition. At 25 fps the distance that is traversed by a RBC from frame to frame can be considerable but if the frame rate could be increased to 500 or 1000 frames per second, then a much better tracking could be obtained.

Another improvement could be obtained by matching the calculated tracks to images of the blood vessels themselves, either from transmitted light images or fluorescence images, where the vessel walls are highlighted by fluorescent marker proteins, emitting at a different wavelength from the RBCs. In this way,

we would be able to ‘see’ the tracks that the RBCs are running on, and restrict the movement of the cells to these vessels.

A final improvement for the algorithm could be to introduce a *reliability criterion*. When the correspondence between objects in consecutive frames is assigned, it is possible to know how many objects landed on the keyhole. If there is more than one, the algorithm selects the one most likely to be correct, which introduces uncertainty on the track. The cumulative uncertainty could be used as a reliability-weighting factor towards the estimation of the mean velocity.

CONCLUSION

A tracking algorithm based on fluorescently labelled red blood cells, window chambers and a keyhole model of movement has been presented. The proposed keyhole model considered two regions for the probable movement of red blood cells, which have been segmented from a fluorescence intensity image, between contiguous frames of a video sequence. The algorithm required minimal user intervention in a series of pre-processing, tracking and post-processing steps that produced a series of three-dimensional tracks that recorded the temporal position of red blood cells that travel through microvessels of tumours. From the tracks, the geometry of the functional vessels can be observed and the velocity together with other measurements can be extracted. The algorithm was tested first with eight tumours with different vasculature geometries and second, on a longitudinal study of velocities performed after administering a vascular disrupting agent to two

tumours. In both cases, the algorithm successfully tracked the cells travelling through the tumour vasculature.

REFERENCES

Acton, S. T., Wethmar, K. & Ley, K. (2002) Automatic tracking of rolling leukocytes in vivo. *Microvasc Res,* **63,** 139-148.

Akerman, S., Kanthou, C., Pettyjohn, K., Barber, P. R., Coralli, C., Dachs, G., Harris, S., Honess, D. J., Hylands, F., Ireson, C., Prise, V., Ruhrberg, C., Shima, D., Steele, A., Wilson, I., Hill, S. A. & Tozer, G. M. (2006) Tumour Cells Expressing only single VEGF Isoforms (120, 164 or 188) For tumours with very different vascular maturities and response to combretastatin A-4-P. *Angiogenesis,* **9,** 28-29.

Algire, G. H. (1943) An adaptation of the transparent-chamber technique to the mouse. *J. Nat. Cancer Inst.,* **4,** 1-11.

Algire, G. H. & Legallais, F. Y. (1949) Recent developments in the transparent-chamber technique as adapted to the mouse. *J Natl Cancer Inst,* **10,** 225-253, incl 228 pl.

Branemark, P. I. & Lindstrom, J. (1963) A modified rabbit's ear chamber; high-power high-resolution studies in regenerated and preformed tissues. *Anat Rec,* **145,** 533-540.

Carmeliet, P. & Collen, D. (2000) Transgenic mouse models in angiogenesis and cardiovascular disease. *Journal of Pathology,* **190,** 387-405.

Cui, J., Acton, S. T. & Lin, Z. (2006) A Monte Carlo approach to rolling leukocyte tracking in vivo. *Med Image Anal,* **10,** 598-610.

Eden, E., Waisman, D., Rudzsky, M., Bitterman, H., Brod, V. & Rivlin, E. (2005) An automated method for analysis of flow characteristics of circulating particles from in vivo video microscopy. *IEEE Trans Med Imaging,* **24,** 1011-1024.

Fukumura, D. & Jain, R. K. (2006) Tumor microenvironment abnormalities: Causes, consequences, and strategies to normalize. *J Cell Biochem*.

Gaede, V. & Günther, O. (1998) Multidimensional access methods. *ACM Computing Surveys,* **30,** 170-231.

Isard, M. & Blake, A. (1998) Condensation- Conditional density propagation for visual tracking. *Int J Computer Vision,* **29,** 5-28.

Jain, R. K. (2005) Normalization of tumor vasculature: an emerging concept in antiangiogenic therapy. *Science,* **307,** 58-62.

Japee, S. A., Pittman, R. N. & Ellis, C. G. (2005) Automated method for tracking individual red blood cells within capillaries to compute velocity and oxygen saturation. *Microcirculation,* **12,** 507-515.

Ji, L. & Danuser, G. (2005) Tracking quasi-stationary flow of weak fluorescent signals by adaptive multi-frame correlation. *J Microsc,* **220,** 150-167.

Lominadze, D. & Mchedlishvili, G. (1999) Red blood cell behaviour at low flow rate in microvessels. *Microvasc. Res.,* **58,** 187-189.

Prazma, J., Carrasco, V. N., Garrett, C. G. & Pillsbury, H. C. (1989) Measurement of cochlear blood flow: intravital fluorescence microscopy. *Hear Res,* **42,** 229-236.

Ray, N., Acton, S. T. & Ley, K. (2002) Tracking leukocytes in vivo with shape and size constrained active contours. *IEEE Trans Med Imaging,* **21,** 1222-1235.

Salmon, W. C., Adams, M. C. & Waterman-Storer, C. M. (2002) Dual-wavelength fluorescent speckle microscopy reveals coupling of microtubule and actin movements in migrating cells. *J Cell Biol,* **158,** 31-37.

Sandison, J. C. (1924) A new method for the microscopic study of living growing tissues by the introduction of a transparent chamber in the rabbit's ear. *Anat. Rec.,* **28,** 281-287.

Shafique, K. & Shah, M. (2005) A noniterative greedy algorithm for multiframe point correspondence. *IEEE Trans Pattern Anal Mach Intell,* **27,** 51-65.

Stalmans, I., Ng, Y. S., Rohan, R., Fruttiger, M., Bouche, A., Yuce, A., Fujisawa, H., Hermans, B., Shani, M., Jansen, S., Hicklin, D., Anderson, D. J., Gardiner, T., Hammes, H. P., Moons, L., Dewerchin, M., Collen, D., Carmeliet, P. & D'Amore, P. A. (2002) Arteriolar and venular patterning in retinas of mice selectively expressing VEGF isoforms. *J Clin Invest,* **109,** 327-336.

Sugii, Y., Nishio, S. & Okamoto, K. (2002) Measurement of a velocity field in microvessels using a high resolution PIV technique. *Ann N Y Acad Sci,* **972,** 331-336.

Tozer, G. M., Ameer-Beg, S. M., Baker, J., Barber, P. R., Hill, S. A., Hodgkiss, R. J., Locke, R., Prise, V. E., Wilson, I. & Vojnovic, B. (2005a) Intravital imaging of tumour vascular networks using multi-photon fluorescence microscopy. *Adv Drug Deliv Rev,* **57,** 135-152.

Tozer, G. M., Kanthou, C. & Baguley, B. C. (2005b) Disrupting tumour blood vessels. *Nat Rev Cancer,* **5,** 423-435.

Tozer, G. M., Prise, V. E., Wilson, J., Cemazar, M., Shan, S., Dewhirst, M. W., Barber, P. R., Vojnovic, B. & Chaplin, D. J. (2001) Mechanisms associated with tumor vascular shut-down induced by combretastatin A-4 phosphate: intravital microscopy and measurement of vascular permeability. *Cancer Res,* **61,** 6413-6422.

Tsukada, K., Minamitani, H., Sekizuka, E. & Oshio, C. (2000) Image correlation method for measuring blood flow velocity in microcirculation: correlation 'window' simulation and in vivo image analysis. *Physiol Meas,* **21,** 459-471.

Tsukada, K., Sekizuka, E., Oshio, C., Tsujioka, K. & Minamitani, H. (2004) Red blood cell velocity and oxygen tension measurement in cerebral microvessels by double-wavelength photoexcitation. *J Appl Physiol,* **96,** 1561-1568.

Unthank, J., Lash, J., Nixon, J., Sidner, R. & Bohlen, H. (1993) Evaluation of carbocyanine-labeled erythrocytes for microvascular measurements. *Microvascular Res,* **45,** 193-210.

Vennemann, P., Kiger, K. T., Lindken, R., Groenendijk, B. C., Stekelenburg-de Vos, S., ten Hagen, T. L., Ursem, N. T., Poelmann, R. E., Westerweel, J. & Hierck, B. P. (2006) In vivo micro particle image velocimetry measurements of blood-plasma in the embryonic avian heart. *J Biomech,* **39,** 1191-1200.

Waterman-Storer, C. M., Desai, A., Bulinski, J. C. & Salmon, E. D. (1998) Fluorescent speckle microscopy, a method to visualize the dynamics of protein assemblies in living cells. *Curr Biol,* **8,** 1227-1230.

Table 1. Number of frames analysed, number of tracks, mean velocity [μm/s] (weighted average), standard deviation, maximum and minimum values of 8 tumour sets.

Tumour		**1**	**2**	**3**	**4**	**5**	**6**	**7**	**8**
Number of frames		500	500	300	327	454	401	454	180
Number of tracks		238	206	30	231	346	261	208	57
E(x)	[μm/s]	203	86	260	162	236	308	131	372
Std	[μm/s]	147	60	188	148	208	219	117	307
Max [E(x)]	[μm/s]	760	264	933	719	967	1082	663	1212
Min [E(x)]	[μm/s]	13	17	43	10	11	7	13	26

Figure 1 Pre-processing of the images from input frames to binary images. (a) One sample frame where several RBCs can be identified together with labels, noise and artefacts (notice the higher intensity at the centre of the image). (b) The mean image of a sequence of 50 frames. (c) Pixel to pixel subtraction of (a) and (b); the difference of the images has eliminated noise, intensity bias as well as labels that are super-imposed on the images. (d) Segmentation of the Red Blood Cells by thresholding. Notice not all RBC are segmented thus only some RBCs will form tracks (e) A zoom into the binary image obtained by thresholding (c). (f) Labelling of (e) to identify unique objects, 4 in this case. It will be the centroids of these objects that will be tracked.

Figure 2 RBC keyhole movement model. (a) It is assumed that between consecutive frames a RBC can move towards any direction and with any distance. (b) Without movement history, the only assumption possible is that its landing prediction will be within a circular region. (c, d) A landing position is predicted assuming constant velocity and direction, this creates two probable regions: a wedge (c) and a circle (d) which when combined create a keyhole model. (e) Two examples of tracks of different velocities.

Figure 3 Tracks obtained for eight different tumours. Each individual RBC track is presented as a line with colours representing the velocities. It can be seen that the velocity in some vessels is consistently faster (red) than in others (blue).

Figure 4 Tracks from 2 tumours with different observation angles. While tracks in figure 3 are projected in time, tracks in 4 (a, b) are projected in one column plane. Faster tracks will have lower slopes than slower tracks. (c,d) Tracks are presented in 3D with x-y dimensions (rows and columns) together with time in the z-axis. In (c) a reduced number of tracks from (a). Notice the track that changes direction in the middle of its path.

Figure 5 Scatter plots of three measurements of the tracks. (a) A Cartesian plot with average velocity of the tracks on the x-axis and the number of frames the track spans on the y-axis. (b, c) Polar plots of two different tumours. The direction of each track determines the angle (0-360º) and the velocity determines its distance from the centre of the plot. Several important observations arise from the plots: longer tracks tend to have lower average velocities since they are formed by more 'hops'. Outliers, that is, tracks whose velocity is beyond a normal distribution, are easily identified (red circle) and can be removed from the data set. General behaviour in terms of direction and velocity of the tumour can be identified from the polar plots

Figure 6 Time curves for the velocities of 2 regions in a tumour expressing VEGF188 (solid blue lines) and 2 regions in tumours expressing VEGF120 (dashed red lines). The velocities were evaluated before the drug CA-4-P was administered and 2.5, 15, 30, 60 minutes 3,6 and 24 hours after administration. While the VEGF120–expressing tumour presents a rapid decrease in the velocity and a complete shutdown by 6 hours, the VEGF188–expressing tumour presents a decrease in flow and then a recovery up to levels similar to the initial state.

Figure 7 Low magnification (2.5x objective) light microscopy of the whole tumours from which time curves of figure 6 were calculated. Top row: VEGF120 tumour at (a) 0 minutes, (b) 60 minutes and (c) 24 hours. Bottom row: VEGF188 tumour at (d) 0 minutes, (e) 60 minutes and (f) 24 hours. The VEGF120 case presents shutdown of the vessels and then haemorrhage and a central necrosis at 24 hours while the VEGF188 presents shutdown of some vessels and then a recovery of the vasculature, which is consistent with the quantitative velocity data shown in figure 6.

Figure 8 The problem of out-of-plane imaging. The two-dimensional images that are obtained from a microscope are essentially 2D projections of a three-dimensional structure. As such, if a cell travels in the third dimension, or 'up-down' this movement is not registered within the projection except perhaps as a change of focus since the cell is leaving the plane at which the microscope is focused. The velocity calculated thus will be a lower-bound estimation.

Figure 9 Variation of the average velocities against two parameters of the algorithm. (a) Shows the velocity when the wedge angle varies from 10º to 100º and (b) shows the velocity when the intensity threshold level varies from 10 to 28. In both cases each line represents the estimation of the mean of the velocity of all tracks of a tumour set. In both cases the tumours with more variation (blue and black lines with diamond a circle markers) are those with lower number of tracks, i.e. those with few RBCs travelling within the vasculature. In the other cases, where more than 200 tracks were generated, the algorithm is fairly robust.

Figure 1

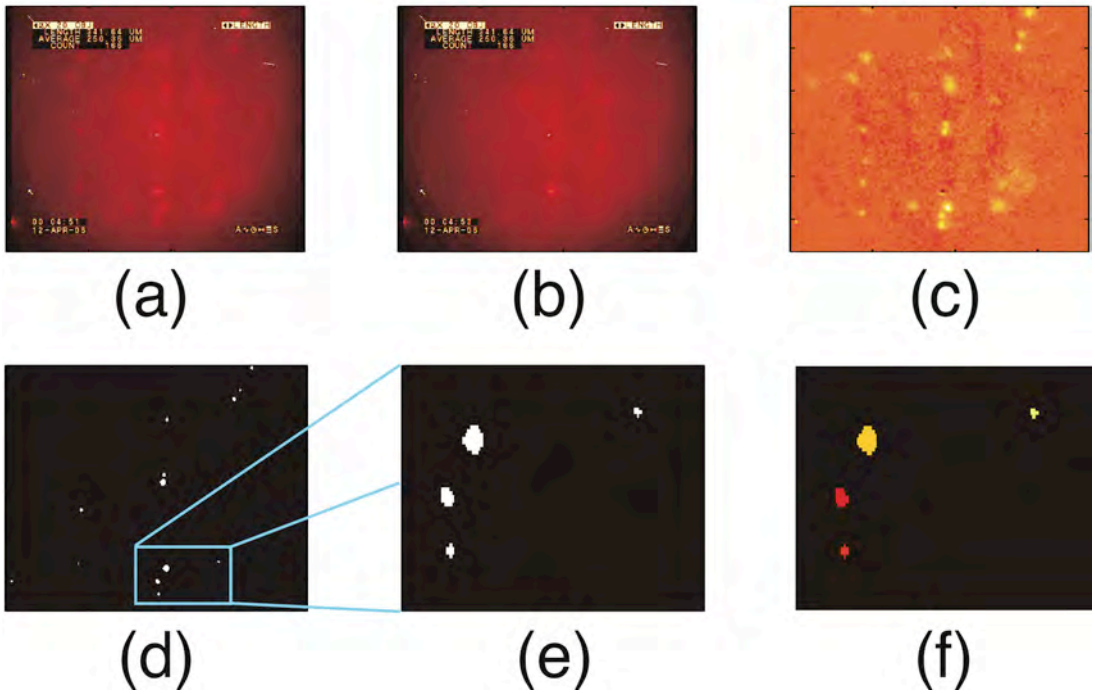

Figure 2

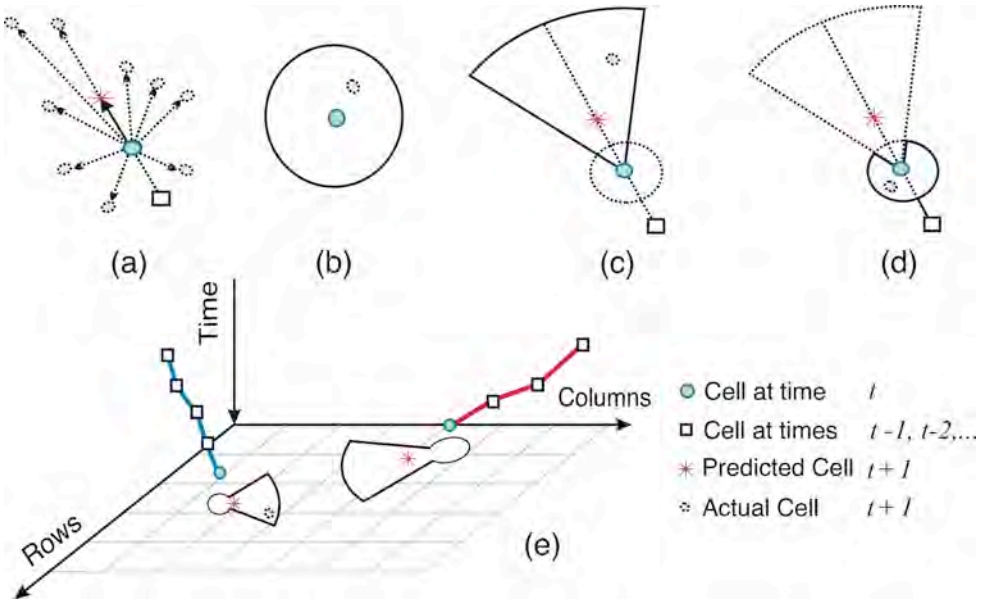

Figure 3

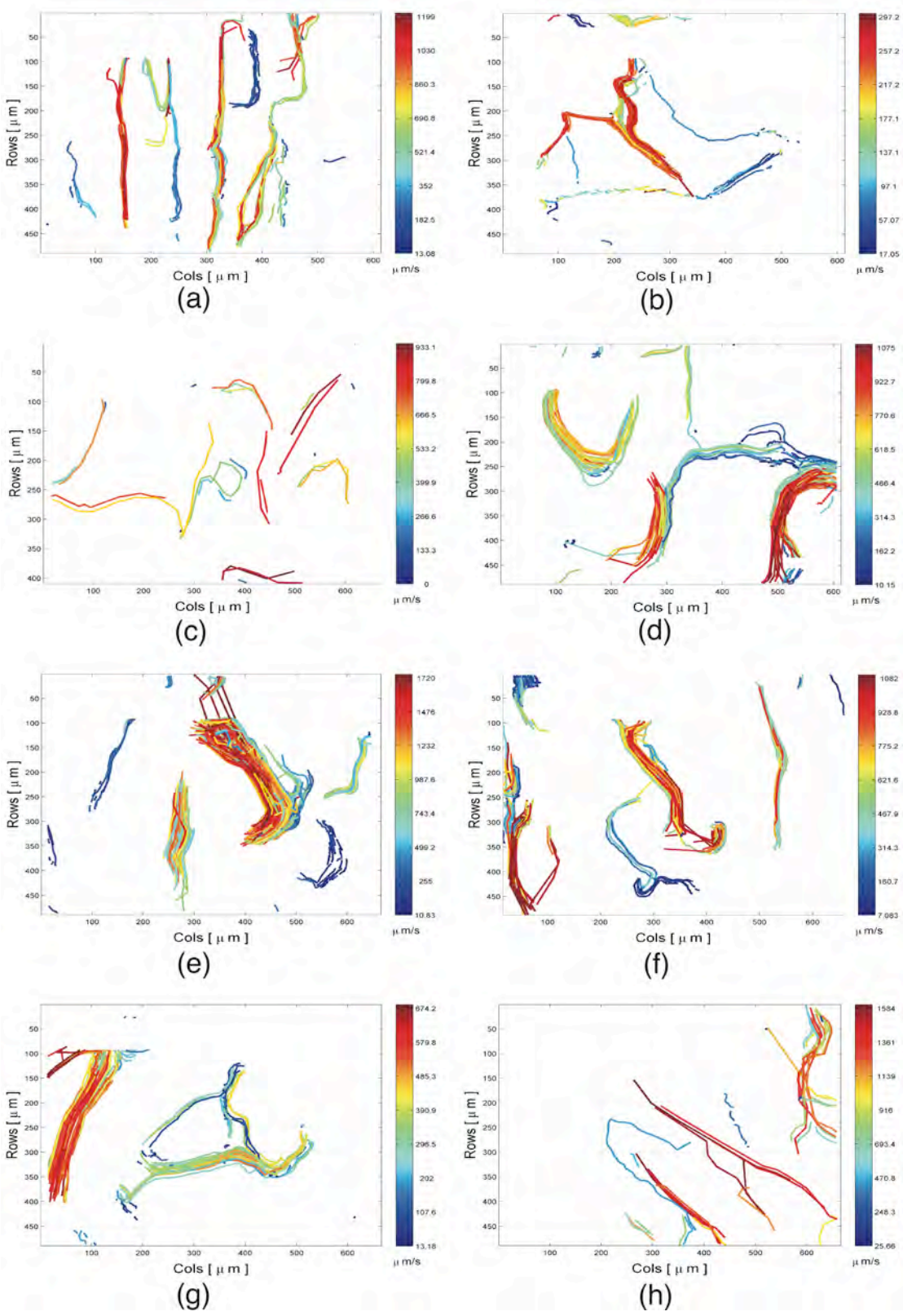

Figure 4

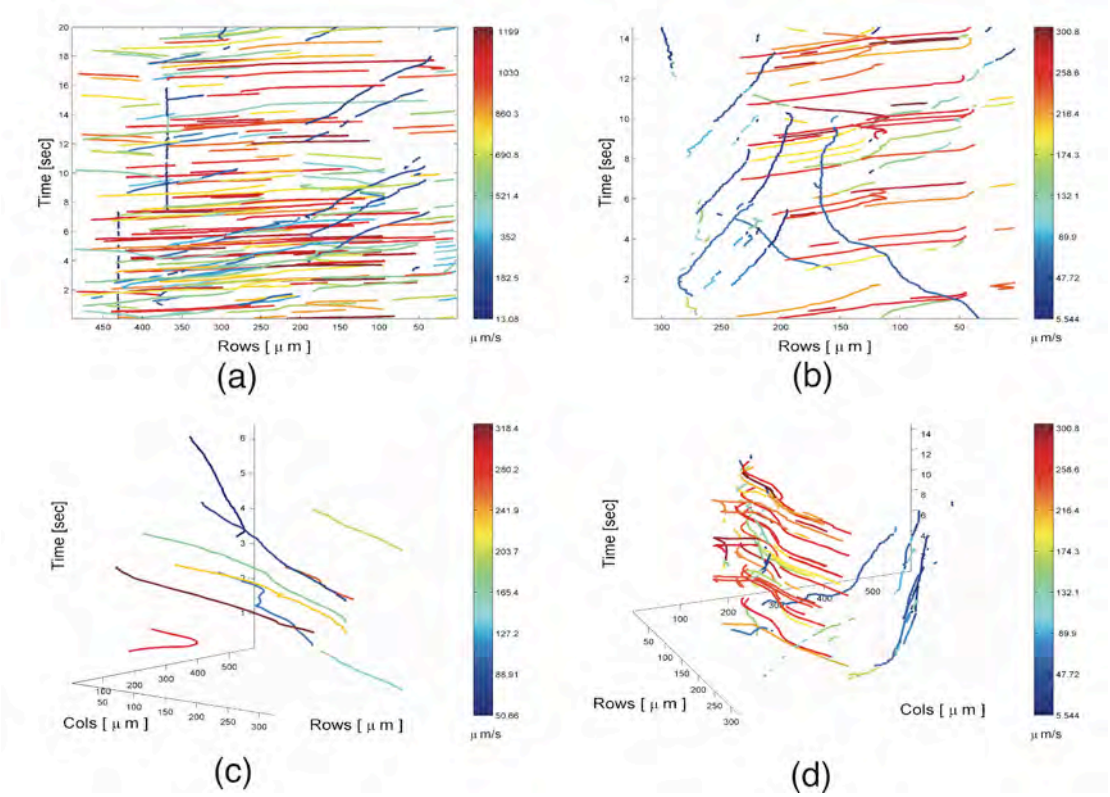

Figure 5

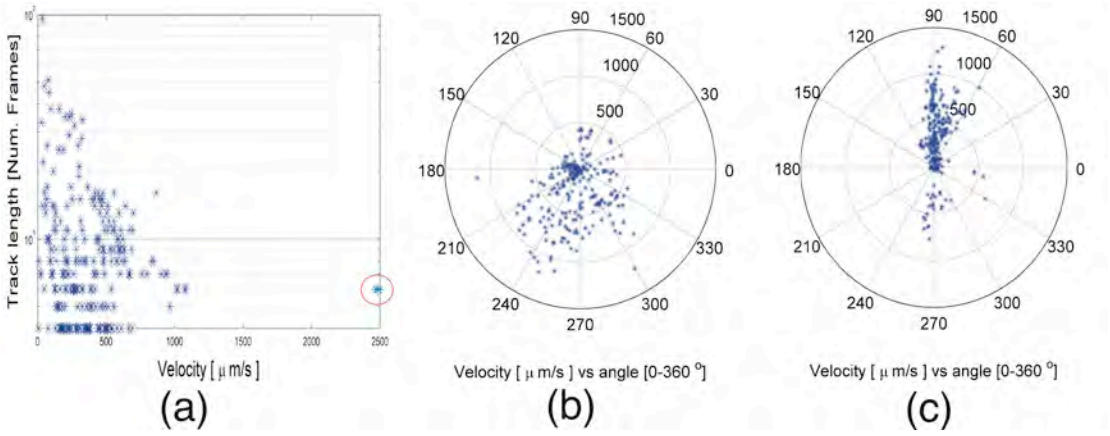

Figure 6

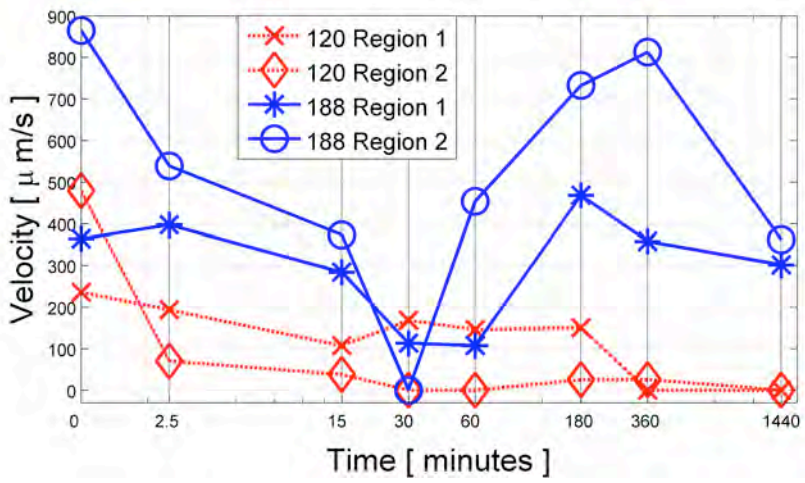

Figure 7

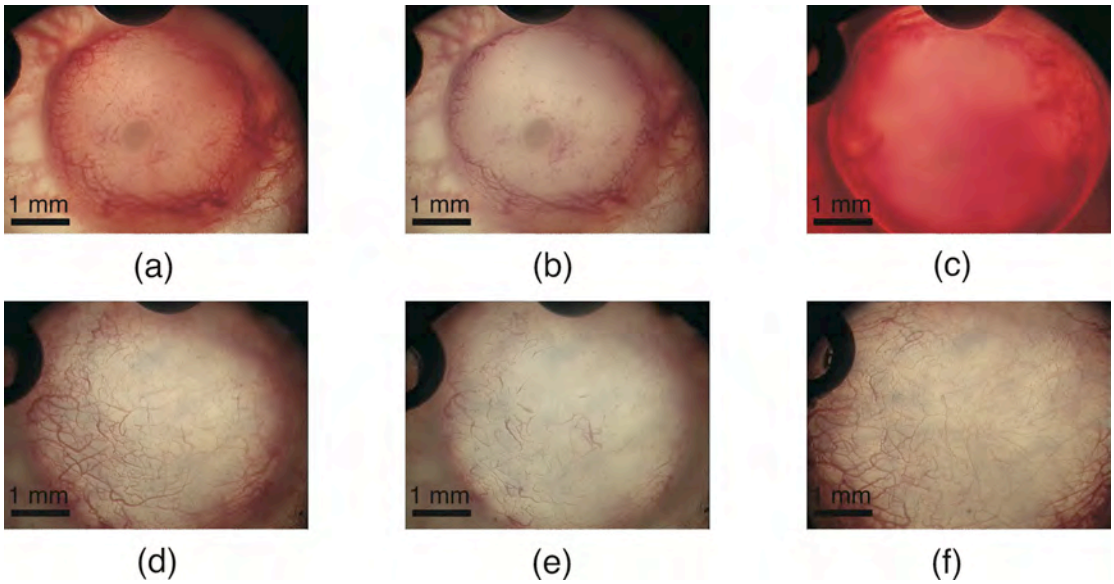

Figure 8

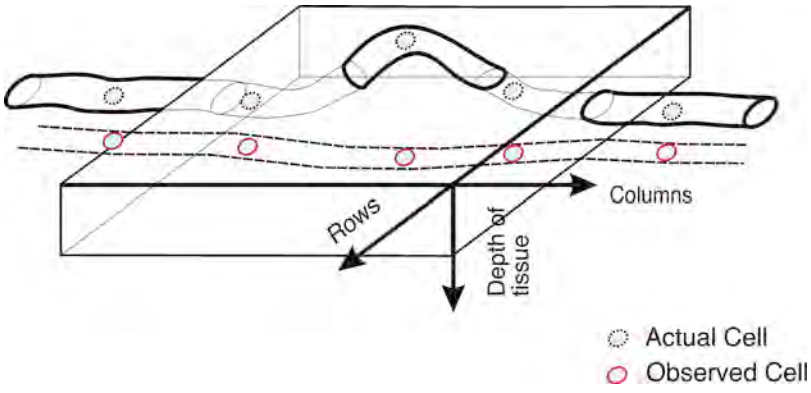

Figure 9

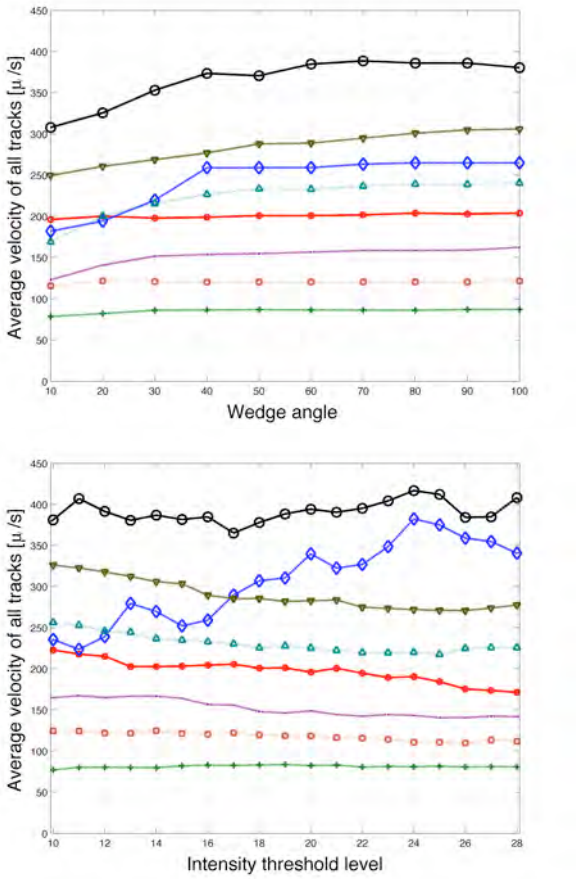
Average velocity of all tracks [μ/s]
Wedge angle
Average velocity of all tracks [μ/s]
Intensity threshold level